

## Supplementary Information

**Stable cycling of Li-S batteries by simultaneously suppressing Li dendrites growth and polysulfides shuttle enabled by a bioinspired separator**

*Yanfei Yang,<sup>a</sup> Wankai Wang,<sup>a</sup> Lingxiao Li,<sup>a</sup> Bucheng Li,<sup>a</sup> and Junping Zhang<sup>\*,a,b</sup>*

<sup>a</sup>Center of Eco-Material and Green Chemistry, Lanzhou Institute of Chemical Physics, Chinese Academy of Sciences, 730000 Lanzhou, P.R. China

<sup>b</sup>Center of Materials Science and Optoelectronics Engineering, University of Chinese Academy of Sciences, Beijing 100049, PR China

\*Corresponding author: [jpzhang@licp.cas.cn](mailto:jpzhang@licp.cas.cn)

## Experimental section

### Materials

TCMS (97%) was purchased from Gelest. S powder and Li<sub>2</sub>S were purchased from Sigma-Aldrich (Shanghai) Co., Ltd. Carbon nanotubes (CNTs, Tube8©) were purchased from JENO, Korea. Dopamine was purchased from Shanghai DEMO Medical Tech Co., Ltd. Toluene, ethanol and Tris were purchased from China National Medicines Co., Ltd. Carbon black and PVDF were purchased from Shenzhen Kejing Star Technology Co., Ltd., China. The electrolyte was purchased from DodoChem, China. All chemicals were used as received without further purification.

### Li<sup>+</sup> conductivity and Li<sup>+</sup> transfer number

The Li<sup>+</sup> conductivity ( $\sigma$ , mS cm<sup>-1</sup>) of the separators was calculated according to the electrochemical impedance spectra of the cells. The cells were composed of two stainless steel electrodes and different separators. The electrochemical impedance spectra of the cells were obtained using an impedance analyzer (CHI660E) at open circuit potential with a constant perturbation amplitude of 5 mV in the frequency range of 0.1-100 KHz, and was calculated based on Fig. S7 using formula:<sup>1</sup>

$$\sigma = \frac{L}{R_b \times A}$$

where  $L$  is the thickness of the separator (cm),  $R_b$  is the bulk resistance ( $\Omega$ ), and  $A$  is the area of the electrode (cm<sup>2</sup>).

The Li<sup>+</sup> transfer number was calculated by a potentiostatic polarization method with a constant potential at 20 mV for 1000 s, and was calculated based on Fig. S8 using formula:<sup>1,2</sup>

$$\text{Li}^+ \text{ transfer number} = \frac{I_s \times (\Delta V - I_o \times R_o)}{I_o \times (\Delta V - I_s \times R_s)}$$

Where  $\Delta V$  is the potentiostatic potential (V),  $R_o$  and  $R_s$  are the resistance before and after the potentiostatic polarization ( $\Omega$ ), respectively,  $I_o$  and  $I_s$  are the current at initial and steady state (mA), respectively.

### **Preparation of Li<sub>2</sub>S<sub>6</sub> solution and polysulfides permeation tests**

A deep red-orange Li<sub>2</sub>S<sub>6</sub> solution was synthesized using S power and Li<sub>2</sub>S with a molar ratio of 5:1 dissolved in DOL/DEM by vigorous stirring for 48 h.

The polysulfides permeation tests were carried out using an H-type device with different separators (Fig. S23). The Li<sub>2</sub>S<sub>6</sub> solution was slowly added into the left glass tube, and a blank DOL/DEM solvent was slowly added into the right glass tube. Before tests, all of the separators were carefully and thoroughly checked to avoid any possible holes and cracks.

### **Characterization**

Surface morphology of the separators was observed via field emission SEM (JSM-6701F, JEOL) and field emission TEM (TECNAI-G2-F30, FEI). Before SEM observation, all samples were fixed on copper stubs using conductive tape and coated with a layer of gold film (ca. 7 nm in thickness). For TEM observation, the samples were prepared as follows. The SNFs/PDA or SNFs on the separators were collected using a knife-peeling method, and then ultrasonically dispersed in ethanol. A drop of SNFs/PDA or SNFs suspension was dropped on a carbon supported copper grid. Fourier Transform infrared (FTIR) spectra of the separators were collected using a Nicolet NEXUS FTIR spectrometer using KBr pellets. XPS spectra of the separators were recorded using a VG ESCALAB 250 Xi spectrometer with a monochromated Al K<sub>α</sub> X-ray radiation source and a hemispherical electron analyzer. The spectra were collected in the constant pass energy mode with a value of 100 eV, and all binding energies were calibrated using the C 1s peak at 284.6 eV as the reference. Raman spectra of separators were recorded using a LabRAM HR Evolution Raman spectrophotometer with a 532 nm laser (HORIBA Jobin Yvon S.A.S. France). For Raman testing, the Celgard@SNFs/PDA separators were washed several times by immersing in pure DOL/DME solvent, and the surface in contact with the cathode facing the laser. Thermostability of the CNTs/S composite was analyzed by thermal gravimetric analysis (TGA) at a heating rate of 10 °C min<sup>-1</sup> in N<sub>2</sub> atmosphere. Thermostability of the separators was analyzed by TGA at a heating rate of 10 °C min<sup>-1</sup> in O<sub>2</sub> atmosphere. The contact angles of electrolyte (10 μL) on the surface of

the separators were collected at 25 °C on a Contact Angle System OCA 20 (Dataphysics, Germany). The dynamic wetting behavior of the separators by electrolyte (6  $\mu$ L) was tested at 4000 fps using a high-speed video camera (FASTCAM Mini UX100, Photron, Japan).

### Supplementary Note 1. Calculation of specific energy density and power density for Li-S batteries<sup>3</sup>

The specific energy density ( $E$ , Wh kg<sup>-1</sup>) was calculated based on specific capacity based on the mass of S ( $C$ , mA h g<sup>-1</sup>) and the S content on the whole CNT/S cathode ( $m$ , wt.%, including Al current collector, CNTs, super P and PVDF). The specific power density ( $P$ , W kg<sup>-1</sup>) was calculated based on the specific energy density at 1.0 C rate and the entire cathode mass. In this work, the average voltage of the low reduction plateau ( $V$ ) is 2.0 V (Fig. S27). The calculations are presented below:

$$m = \frac{\text{areal density of S}}{\text{areal density of entire cathode}} \times 100\% = \frac{4.3 \text{ mg cm}^{-2}}{14.6 \text{ mg cm}^{-2}} \times 100\% \approx 29.5\%$$

$$E = C \times m \times V = C \times 29.5 \text{ wt. \%} \times 2.0 \text{ V}$$

$$P = E \times C_{\text{rate}} = E \times 1.0 \text{ h}^{-1}$$

For Li-S battery with the Celgard@SNFs/PDA separator and CNTs/S cathode, at the 1<sup>st</sup> cycle,  $E$  and  $P$  are presented below:

$$E = 964.8 \text{ mA h g}^{-1} \times 29.5 \text{ wt. \%} \times 2.0 \text{ V} = 569.2 \text{ Wh kg}^{-1}$$

$$P = 569.2 \text{ Wh kg}^{-1} \times 1.0 \text{ h}^{-1} = 569.2 \text{ W kg}^{-1}$$

At the 1000<sup>th</sup> cycle,  $E$  and  $P$  are presented below:

$$E = 787.6 \text{ mA h g}^{-1} \times 29.5 \text{ wt. \%} \times 2.0 \text{ V} = 464.7 \text{ Wh kg}^{-1}$$

$$P = 464.7 \text{ Wh kg}^{-1} \times 1.0 \text{ h}^{-1} = 464.7 \text{ W kg}^{-1}$$

## Supplementary Note 2. Mechanism of Li dendrites inhibiting

In Li metal battery, the Li metal anode will undergo electrochemical stripping/plating.<sup>4</sup> Li<sup>+</sup> ions are electrochemically reduced and plated on the surface of Li metal anode, and then grow into Li dendrites. Some recent studies have shown that the Li dendrites tend to grow along the tip of the dendrites (Fig. S3a) due to the potential difference between the base and the tip of the dendrites, which acts as the driving force for Li dendrites growth.<sup>5</sup> The main causes for Li dendrites growth are the slow Li<sup>+</sup> diffusion and non-uniform Li<sup>+</sup> flux at the interface of the Li metal anode and the separator.<sup>6</sup>

For the Celgard separator, the Li<sup>+</sup> conductivity is low (0.545 mS cm<sup>-1</sup>) and is due to the filled electrolyte in its pores.<sup>7</sup> The Celgard separator has many non-uniform pores with size up to several hundreds of nanometers (Fig. S2), which leads to extremely non-uniform Li<sup>+</sup> flux after passing through the separator (Fig. S3a). Thus, Li dendrites growth is very serious in Li metal batteries with the Celgard separator.

Different from the Celgard separator, the 3D crosslinked network of the Celgard@SNFs/PDA separator can hold more electrolyte, expanding the pathways for Li<sup>+</sup> transport and decreasing the interfacial resistance. Moreover, the abundant O, N-containing groups of the separator could bond with Li<sup>+</sup> via polar-polar interaction,<sup>8</sup> and then facilitate fast Li<sup>+</sup> diffusion and uniform Li<sup>+</sup> flux (Figs. 2e and S3b). Meanwhile, the abundant Si-O groups (Lewis acid sites) of the separator could trap Li salt anions, and then enhance the Li<sup>+</sup> conductivity and Li<sup>+</sup> transfer number.<sup>8, 9</sup> Thus, the Celgard@SNFs/PDA can redistribute the Li<sup>+</sup> in electrolyte at the molecular level to obtain fast Li<sup>+</sup> diffusion and uniform Li<sup>+</sup> flux at the interface of the Li metal anode and the separator (Fig. S3b). Different from forcing Li dendrites to stop growing by using separators with high mechanical modulus,<sup>10</sup> the Celgard@SNFs/PDA separator inhibits Li dendrites growth by fast Li<sup>+</sup> diffusion and uniform Li<sup>+</sup> flux, which ensures long-term reversible electrochemical stripping/plating even at high current density.

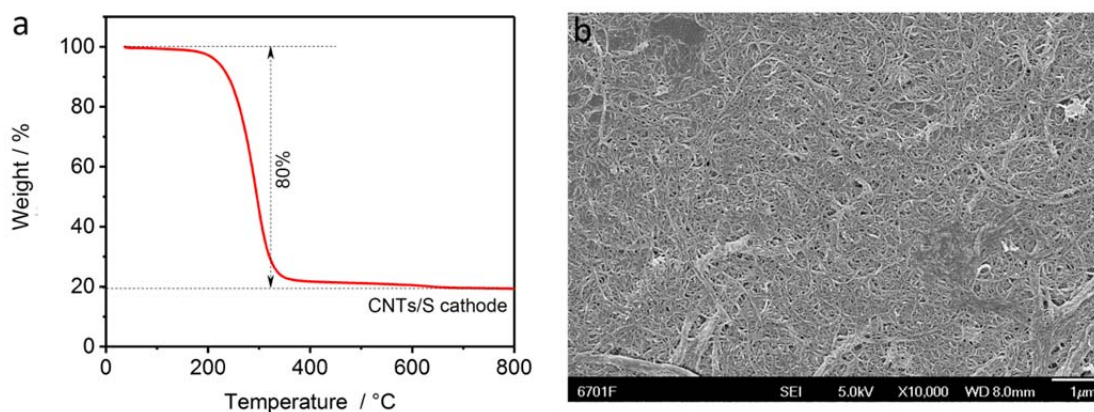


**Fig. S1** (a) TGA curve and (b) SEM image of the CNTs/S composite. The TGA curve was obtained at a heating rate of  $10\text{ }^{\circ}\text{C min}^{-1}$  in  $\text{N}_2$  atmosphere.

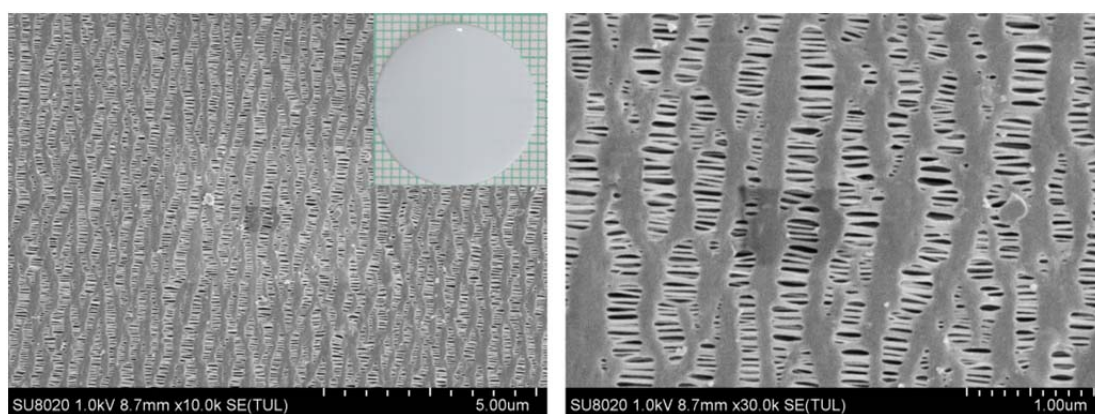


**Fig. S2** SEM images of the Celgard separator. The inset is the photograph of the separator.

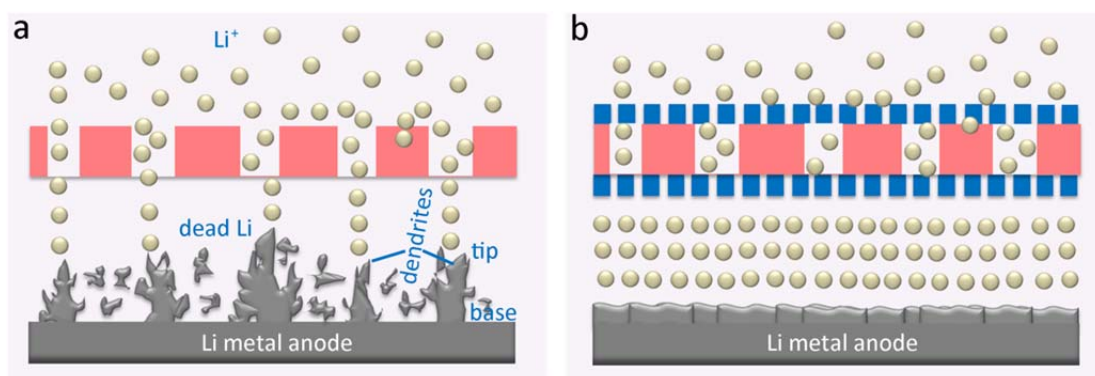


**Fig. S3** Schematic illustrations of the electrochemical plating behaviors of Li metal anodes with (a) the Celgard separator and (b) the Celgard@SNFs/PDA separator.

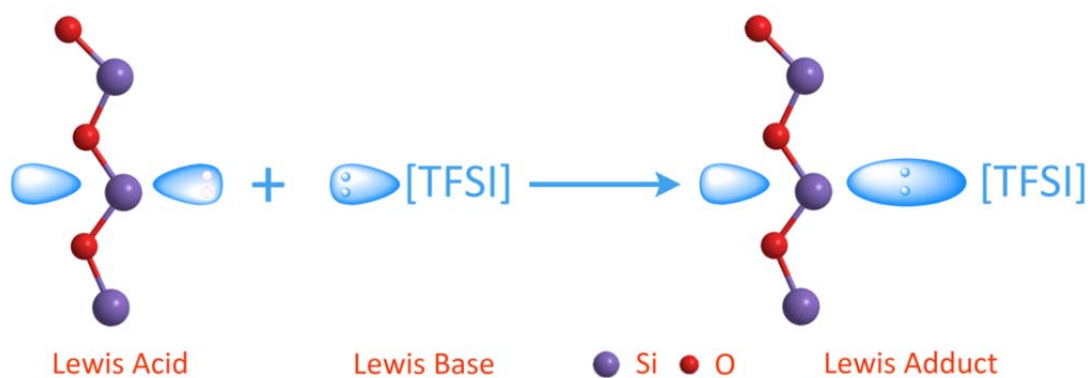


**Fig. S4** Schematic illustration of the interaction between Si-O groups (Lewis acid) and Li salt anions (Lewis base).

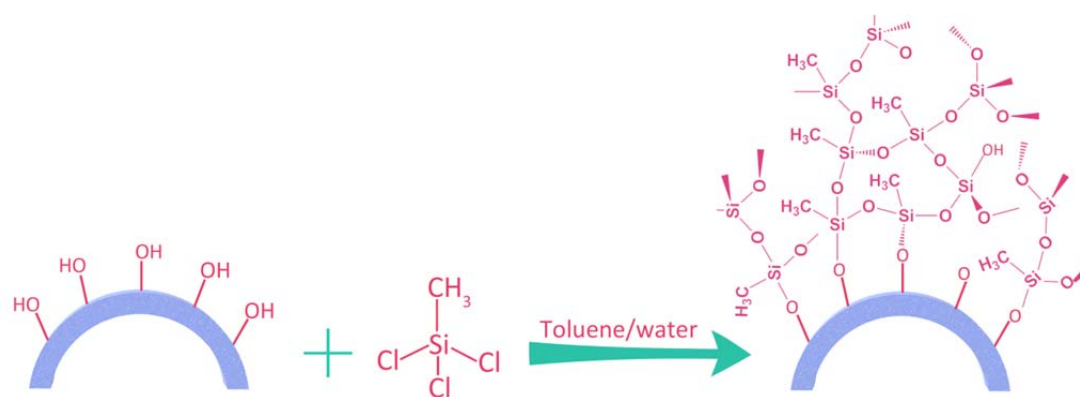


**Fig. S5** Preparation of the Celgard@SNFs separator.

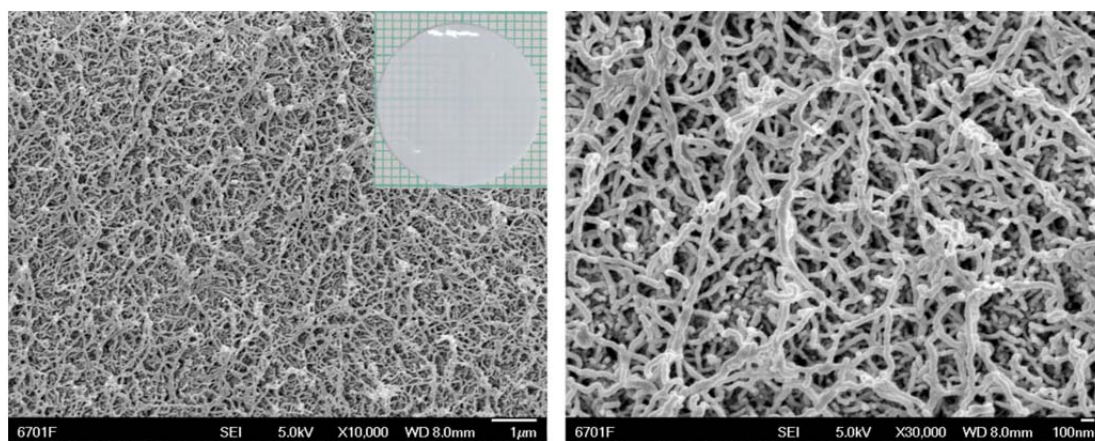


**Fig. S6** SEM images of the Celgard@SNFs separators. The inset is the photograph of the separator.

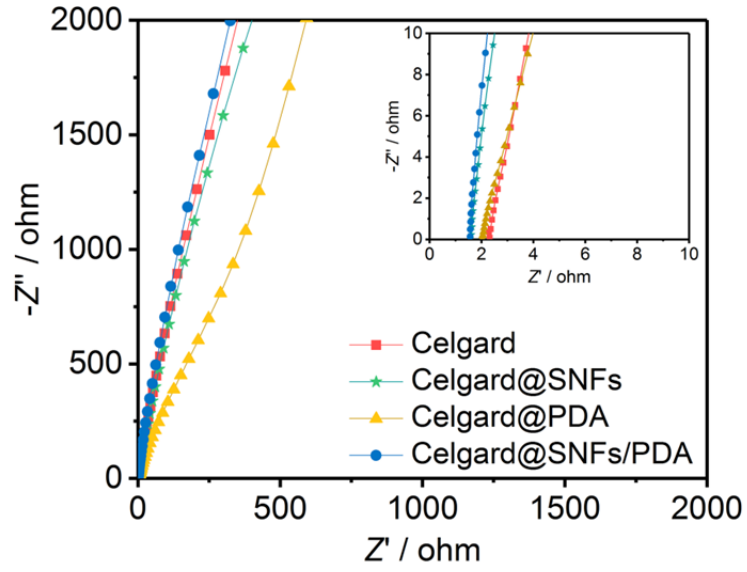


**Fig. S7** Impedance plots of the cells with different separators.

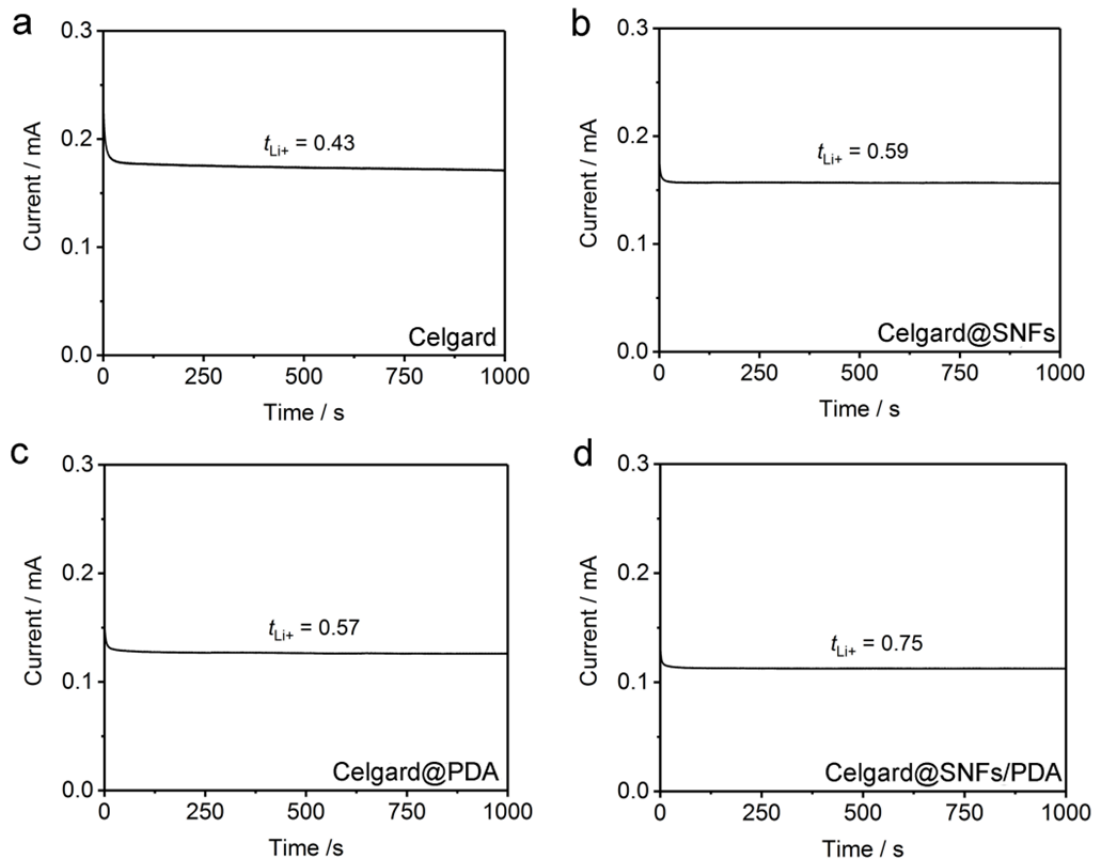


**Fig. S8**  $\text{Li}^+$  transfer number of different separators.

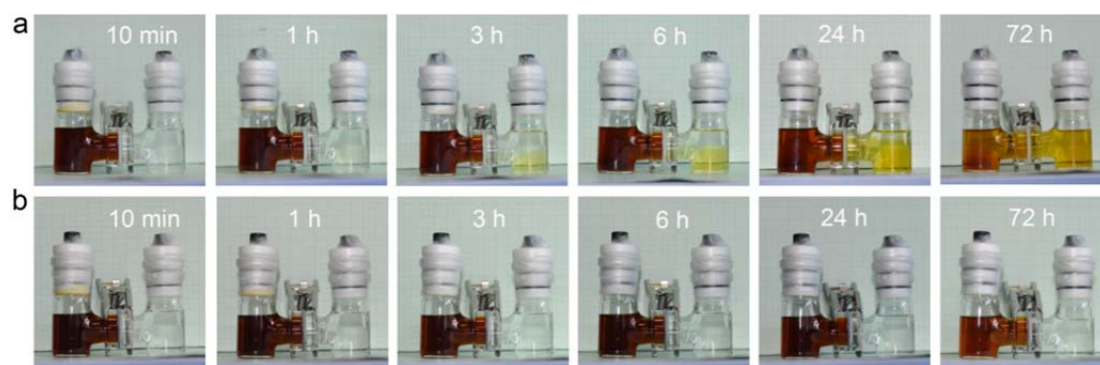


**Fig. S9** Polysulfides permeation tests of the (a) Celgard@SNFs and (b) Celgard@PDA separators using an H-type device.

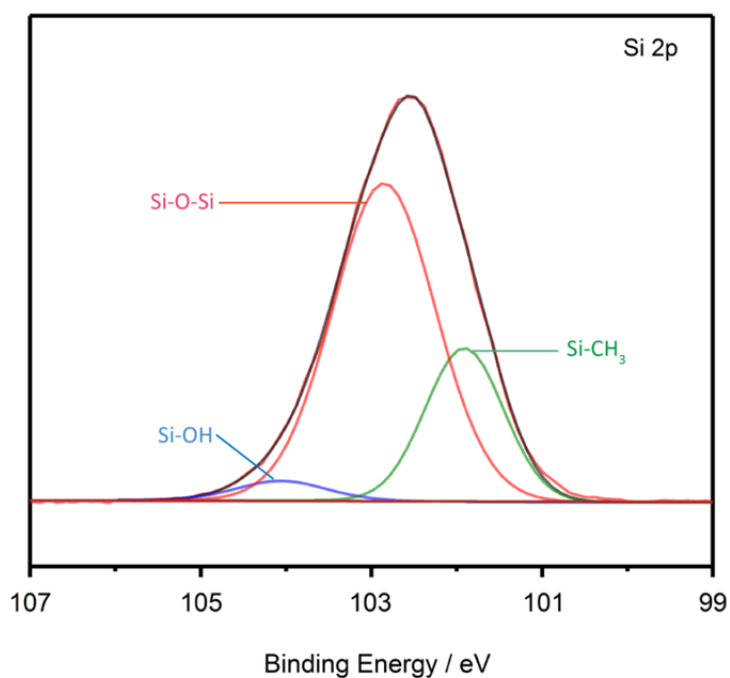


**Fig. S10** Si 2p XPS spectrum of the Celgard@SNFs separator.

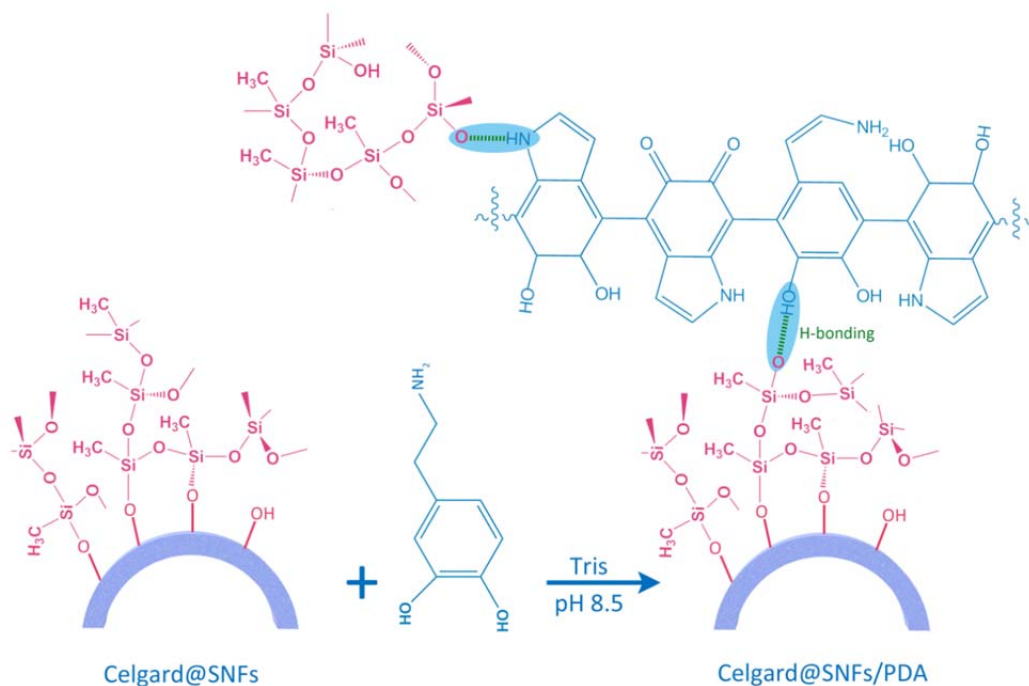


**Fig. S11** Interactions between PDA and SNFs on the Celgard@SNFs/PDA separator.

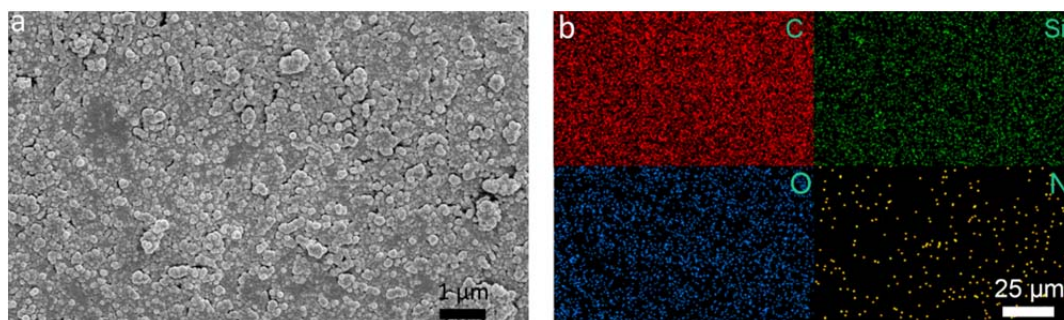


**Fig. S12** (a) SEM image and (b) elemental maps of the Celgard@SNFs/PDA separator.

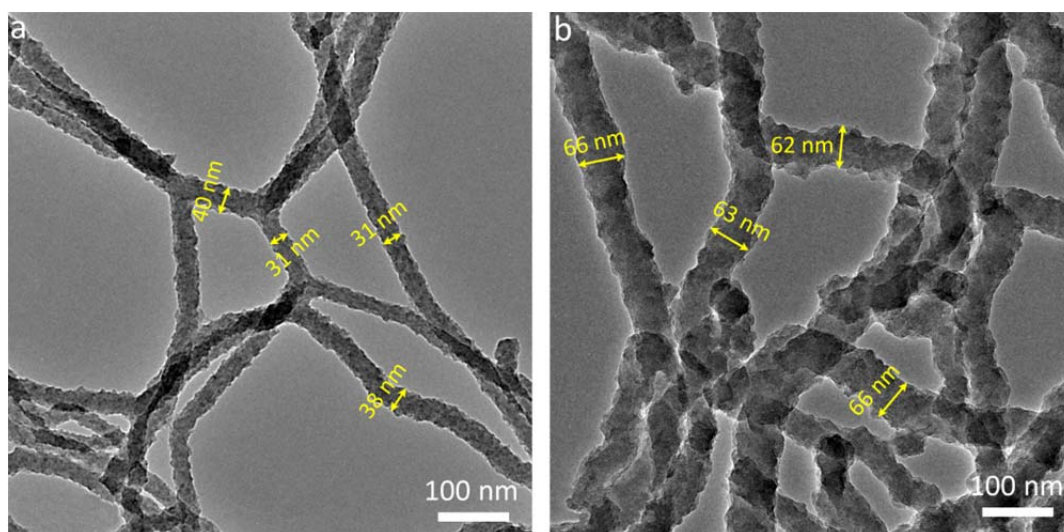


**Fig. S13** TEM images of (a) SNFs on the Celgard@SNFs separator and (b) SNFs/PDA on the Celgard@SNFs/PDA separator.

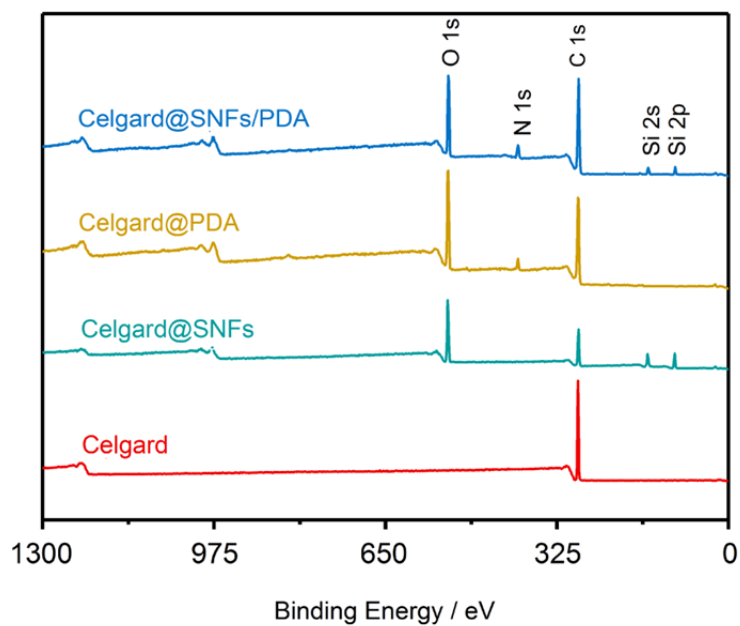


**Fig. S14** XPS spectra of different separators.

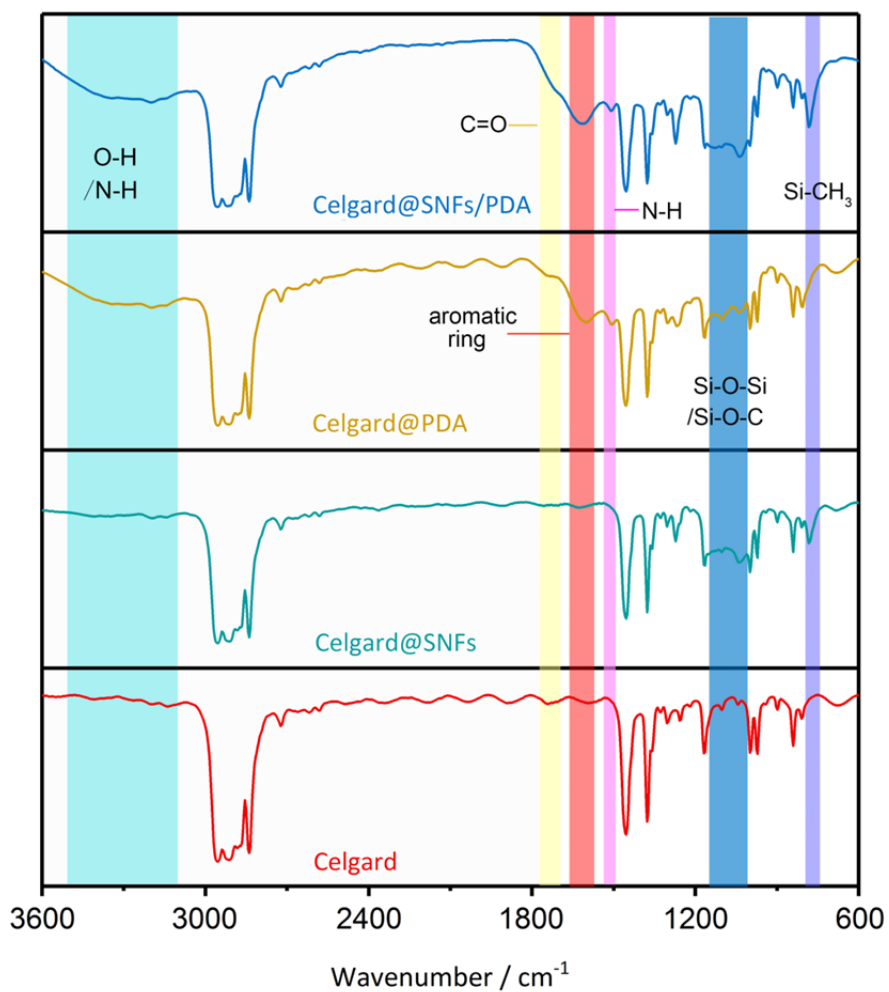


**Fig. S15** FTIR spectra of different separators.

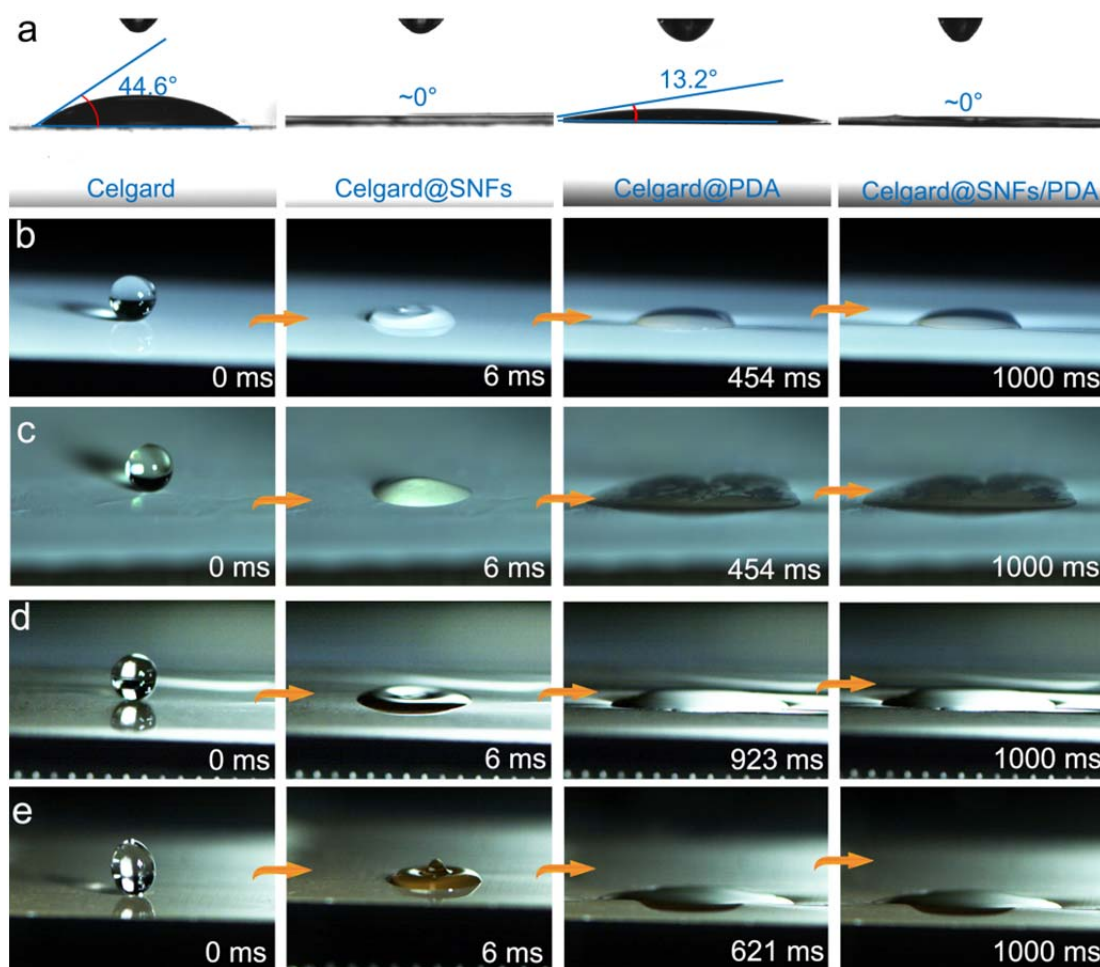


**Fig. S16** (a) Contact angles of electrolyte (10  $\mu\text{L}$ ) on different separators. Dynamic wetting process of the (b) Celgard, (c) Celgard@SNFs, (d) Celgard@PDA, and (e) Celgard@SNFs/PDA separators by 6  $\mu\text{L}$  electrolyte droplets released from a height of 5 mm. The electrolyte droplet wetted and diffused into the Celgard@SNFs/PDA separator in  $\sim 621$  ms, which is faster than the Celgard separator ( $> 1000$  ms) and the Celgard@PDA (923 ms) separator.

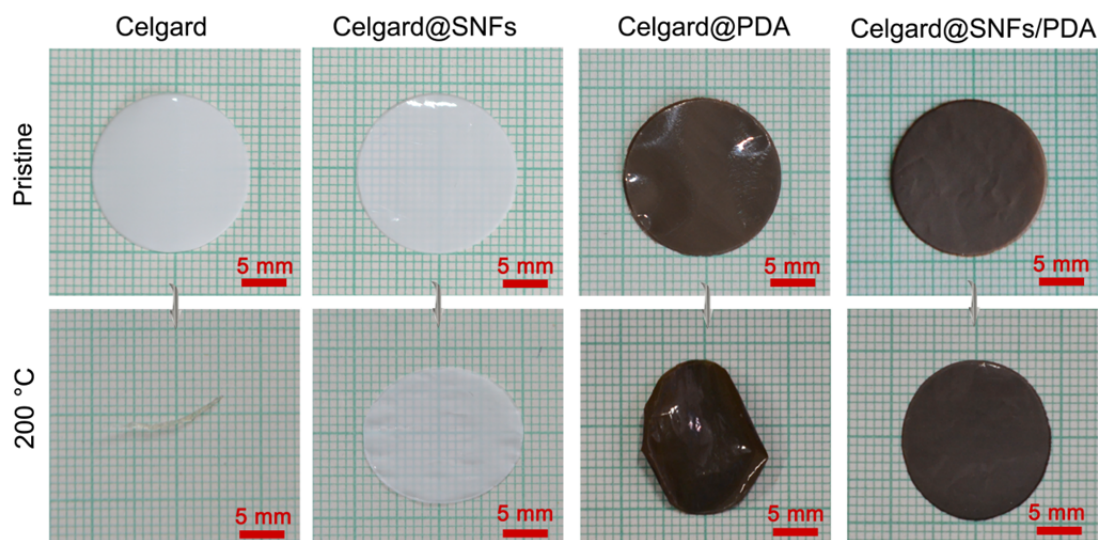


**Fig. S17** Dimension of different separators before and after heat treatment at 200 °C in an oven for 1 h.

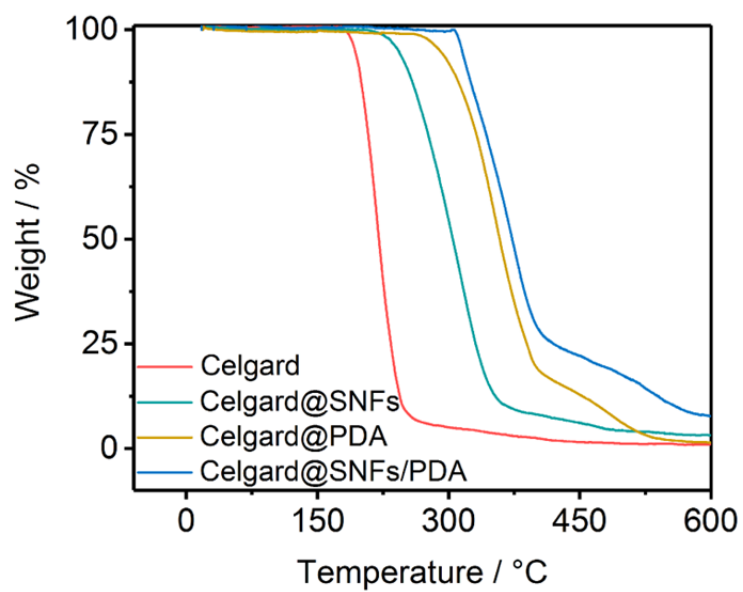


**Fig. S18** TGA curves of different separators at a heating rate of 10 °C min<sup>-1</sup> in O<sub>2</sub> atmosphere.

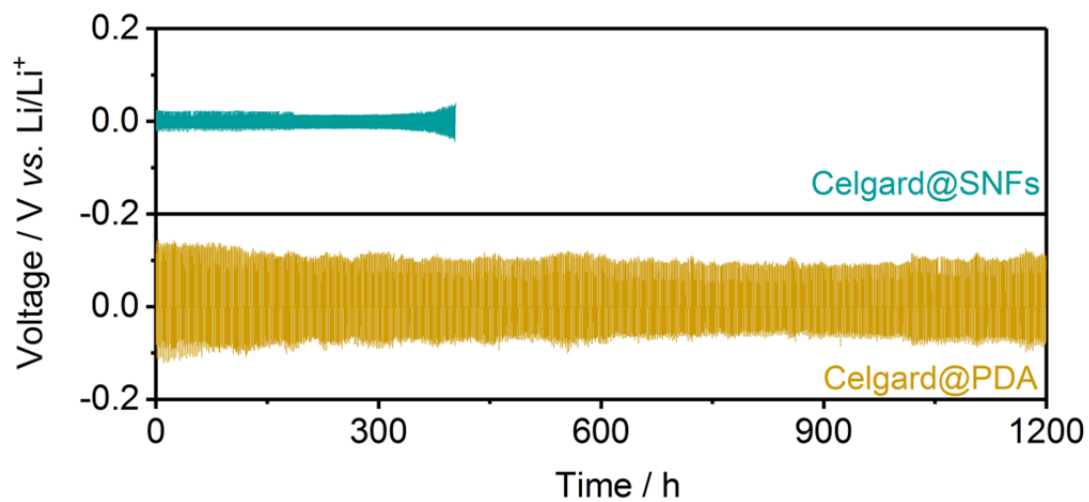


**Fig. S19** Charge/discharge voltage profiles of Li/Li cells with the Celgard@SNFs and Celgard@PDA separators at a current density of  $1.0 \text{ mA cm}^{-2}$  with areal capacity of  $1.0 \text{ mA h cm}^{-2}$ .

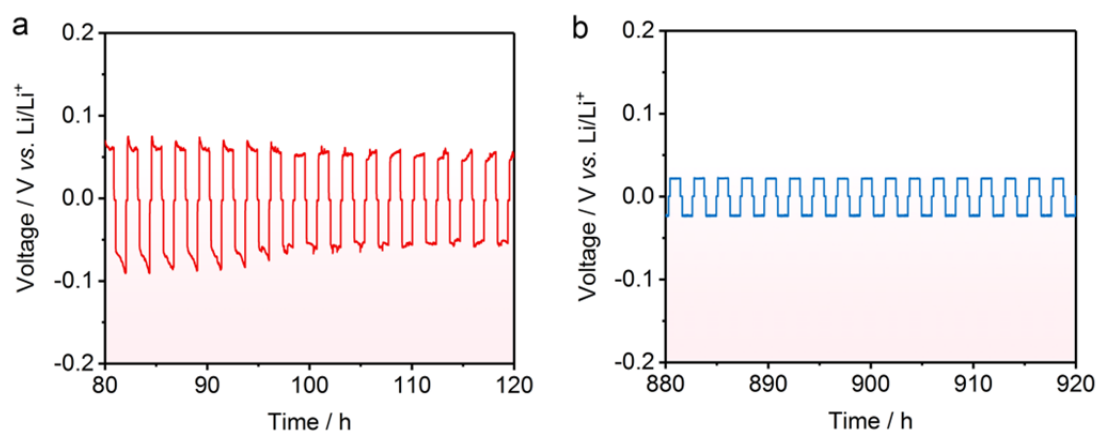


**Fig. S20** Selected voltage profiles of Li/Li cells with the (a) Celgard and (b) Celgard@SNFs/PDA separators.

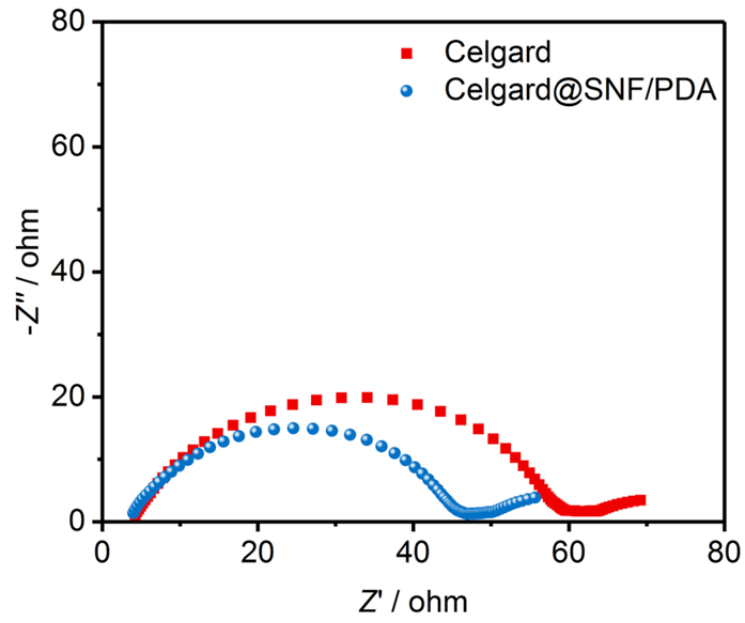


**Fig. S21** Impedance spectra of the Li/Li cells before cycling.

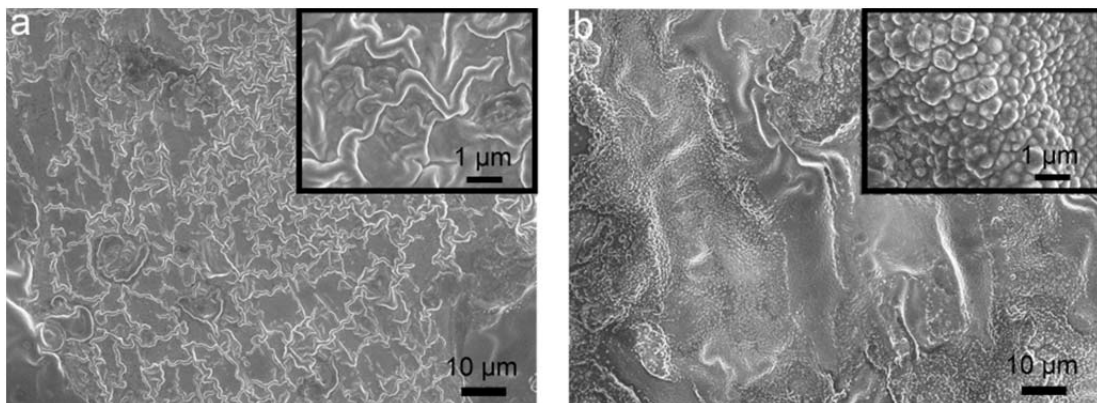


**Fig. S22** SEM images of the cycled Li metal anode in Li/Li cells with the (a) Celgard@SNFs and (b) Celgard@PDA separators.

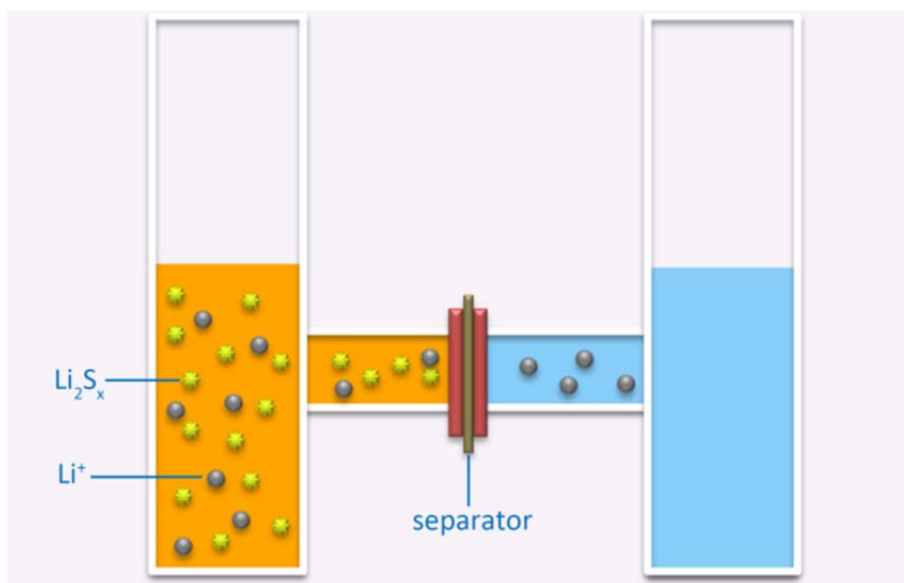


**Fig. S23** Schematic illustration of polysulfides permeation tests through different separators.

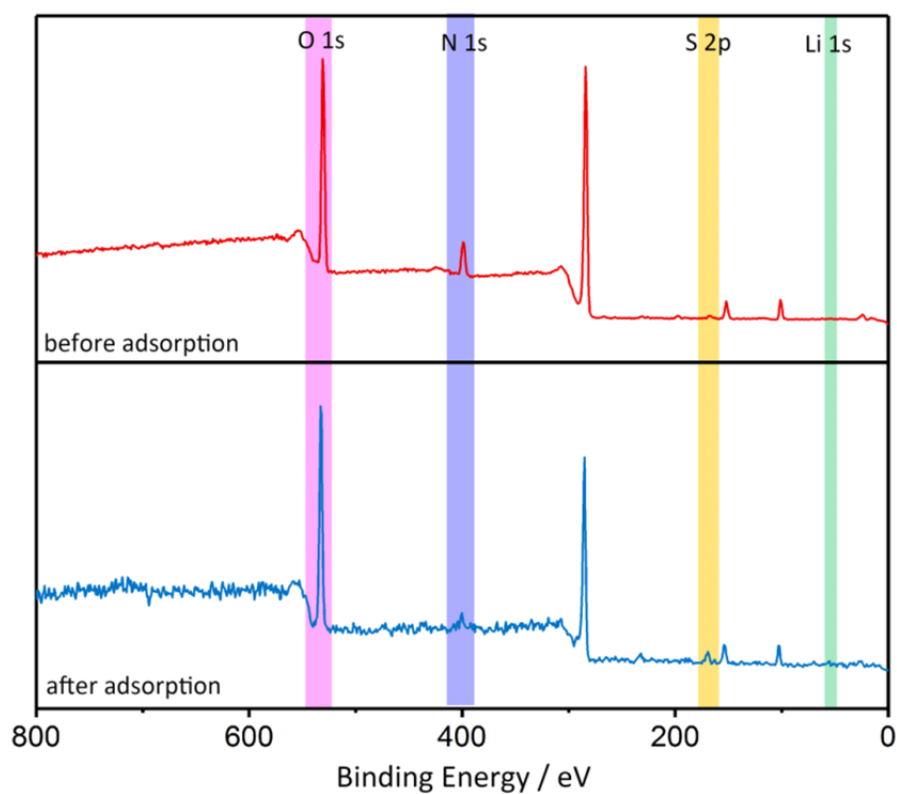


**Fig. S24** XPS spectra of the Celgard@SNFs/PDA separator before and after polysulfides adsorption. After polysulfides adsorption, the Celgard@SNFs/PDA separator was rinsed with 10 mL of DOL/DEM for several times before recording the XPS spectrum.

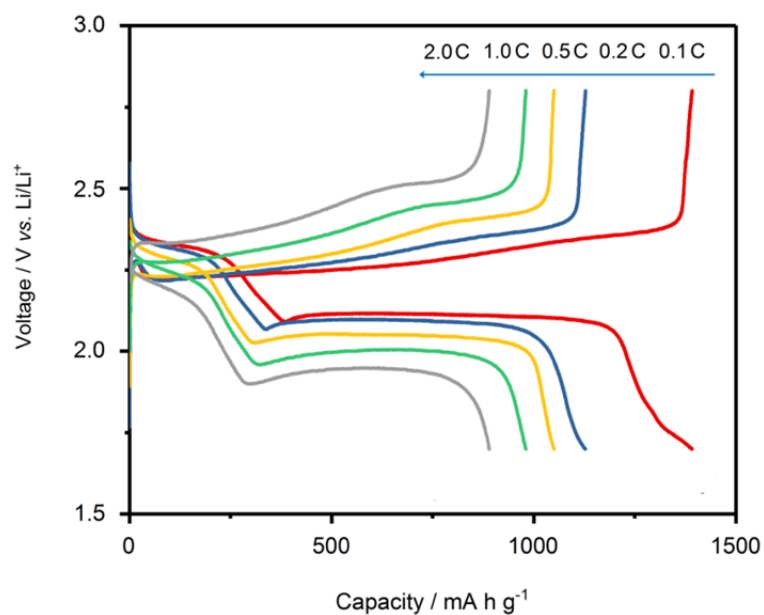


**Fig. S25** Galvanostatic charge/discharge profiles of Li-S battery with the Celgard@SNFs/PDA separator at different rates.

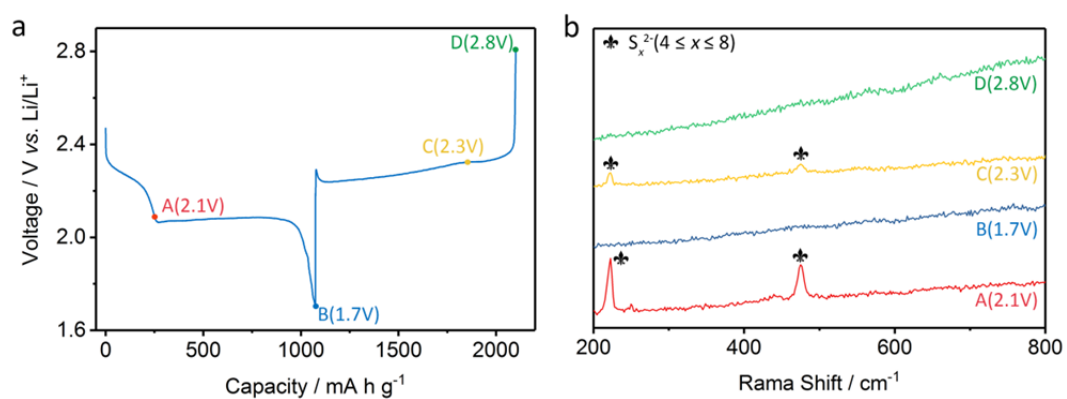


**Fig. S26** (a) First galvanostatic charge/discharge profiles of the Li-S battery with the Celgard@SNFs/PDA separator at 0.2 C and (b) the corresponding Raman spectra of the cycled Celgard@SNFs/PDA separators at different charged states.

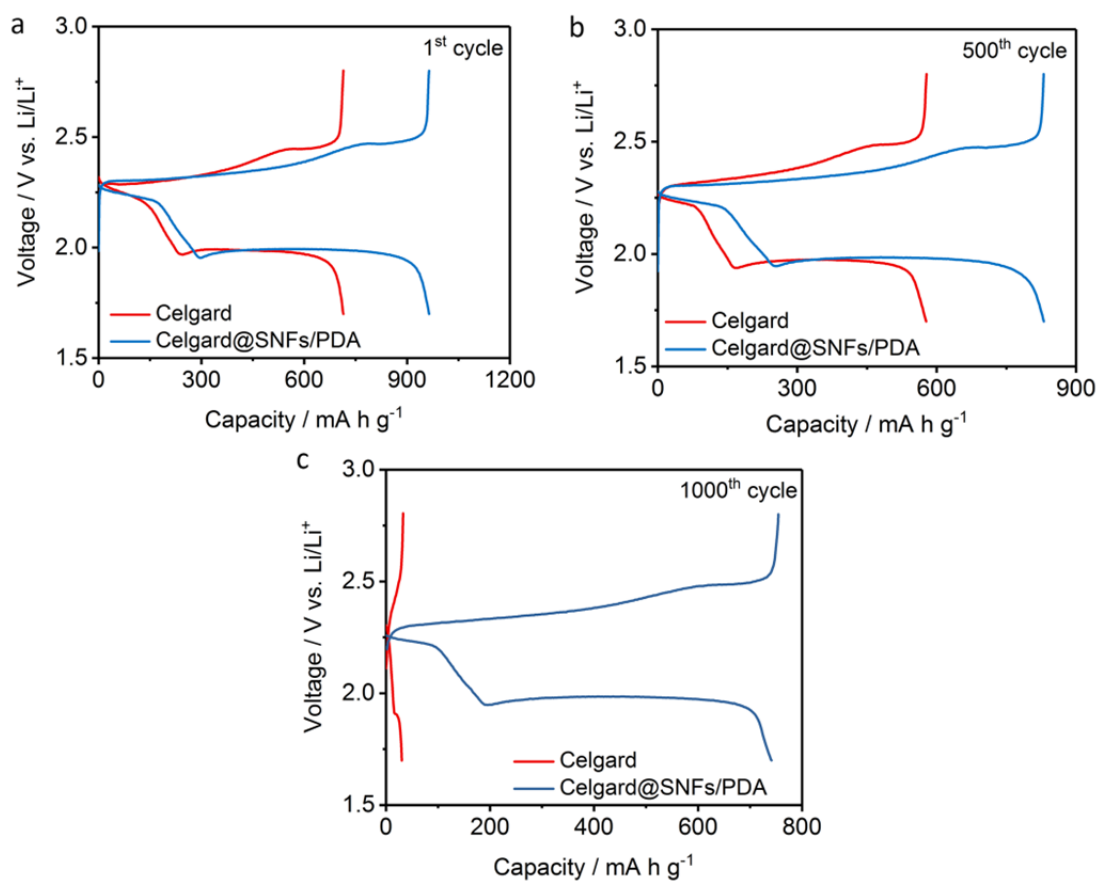


**Fig. S27** Galvanostatic charge/discharge profiles of Li-S batteries with CNTs/S cathode and different separators at 1.0 C: (a) 1<sup>st</sup> cycle, (b) 500<sup>th</sup> cycle and (c) 1000<sup>th</sup> cycle.

**Table S1.** Physical and electrochemical parameters of different separators.

Separators	Li <sup>+</sup> conductivity / mS cm <sup>-1</sup>	Li <sup>+</sup> transfer number	LE uptake / %
Celgard	0.545	0.43	97.2
Celgard@SNFs	0.940	0.59	276.1
Celgard@PDA	0.562	0.51	113.7
Celgard@SNFs/PDA	0.991	0.75	215.1

**Table S2.** Impedance characteristics of Li/Li cells with different separators after cycling.

Separators	Celgard (after 630 h)	Celgard@SNFs/PDA (after 2336 h)
R1 / $\Omega$	368.1	8.2
R2 / $\Omega$	1926.0	94.0
R3 / $\Omega$	7.9	2.2

Equivalent circuit

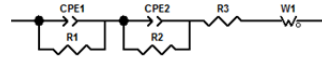


**Table S3.** Performance of Li-S batteries with different separators and pure S cathode in this study and previously reported studies. (“-” means not mentioned).

Coating materials	Simultaneously suppressing Li dendrites growth and polysulfides shuttle?	Li <sup>+</sup> diffusion	Weight of coating / mg cm <sup>-2</sup>	S / wt.%	Cycling stability			Rate performance / mA h g <sup>-1</sup>	Ref.	
					Cycle number	Initial capacity / m Ah g <sup>-1</sup>	Decaying rate / (% per cycle)			
SNFs/PDA	Yes	improved	0.075	70	200	1136.5	0.038	0.2	899.3 (2.0 C)	This work
SNFs/PDA	Yes	improved	0.075	70	1000	982.2	0.025	1.0		This work
MoS <sub>2</sub> /Polymer	Yes	improved	0.1	60	2000	1007	0.029	1.0	766 (3.0 C)	11
LNS/CB	No	improved	0.7	70	500	881	0.028	1.0	753 (2.0 C)	12
BaTiO <sub>3</sub>	No	-	2.4	60	50	1122	0.34	0.1	-	13
MoP <sub>2</sub> &CNT	No	-	>0.3	50	100	1223	0.152	0.2	521 (2.0 C)	14
Black P	No	-	0.4	80	100	930	0.140	0.2	623 (2.1C)	15
MoS <sub>2</sub>	No	improved	-	65	600	808	0.083	0.5	550 (1.0 C)	16
COF/CNT	No	-	-	75	200	~1130	0.13	0.2	820 (2.0 C)	17
BN-Carbon	No	-	-	60	250	1018.5	0.09	0.5	702 (4.0 C)	18

**Table S4.** Performance of Li-S batteries with different S composite cathodes in this study and previously reported studies.

Host materials	S content / wt.%	S loading / mg cm <sup>-2</sup>	Cycling Stability			Ref.
			Rate / C	Cycle Number	Capacity / m Ah g <sup>-1</sup>	
CNTs	64	4.3	1.0	1000 <sup>th</sup>	787.6	This Work
MOFs/CNT film	40	1.0	0.2	500 <sup>th</sup>	758	19
Mesoporous TiN	50	1.0	0.5	500 <sup>th</sup>	644	20
CNT-PEI hybrids	56	1.2	1.0	100 <sup>th</sup>	680	21
N-doped hollow porous carbon spheres	49	1.1-1.5	1.0	400 <sup>th</sup>	706	22
Hierarchical porous carbon rods	63	1.5	0.2	300 <sup>th</sup>	700	23
N-doped graphitic carbon-Co composite	49	2.0	1.0	500 <sup>th</sup>	625	24
Nanoporous graphitic carbon nitride	60	3.0	0.2	175 <sup>th</sup>	~600	25
Co(OH) <sub>2</sub> @LDH	52.5	3.0	0.5	100 <sup>th</sup>	491	26
Hollow carbon nanofibers filled with MnO <sub>2</sub>	49.7	3.5	0.5	300 <sup>th</sup>	662	27
Hollow Carbon spheres and graphene	62	3.9	0.2	200 <sup>th</sup>	520	28
Carbon nanofibers	72	4.5	0.2	200 <sup>th</sup>	680	29
N,S-codoped graphene sponge	63-72.5	4.6	0.5	500 <sup>th</sup>	550	30
CNT	70	6.0	0.5	400 <sup>th</sup>	793	31

**Table S5.** Performance of Li-S batteries with different separators and S composite cathodes in this study and previously reported studies. (“-” means not mentioned).

Coating materials	Simultaneously suppressing dendrites and polysulfides shuttle?	Li <sup>+</sup> diffusion	Weight of coating / mg cm <sup>-2</sup>	S loading / mg cm <sup>-2</sup>	S content / wt.%	Cycling stability					Ref.
						Cycle number	Initial capacity / m Ah g <sup>-1</sup>	Capacity retention / m Ah g <sup>-1</sup>	Decaying rate / (% per cycle)	Rate / C	
SNFs/PDA	Yes	improved	0.075	4.3	64	1000	964.8	787.6	0.018	1.0	This work
Li <sub>4</sub> Ti <sub>5</sub> O <sub>12</sub> /graphene	No	-	~0.35	1.2	60	500	~814	697	~0.029	1.0	32
HKUST-5/GO	No	-	0.3	0.6-0.8	56	1500	1207	855	0.019	1.0	33
CNT@ZIF	No	-	0.9	1.2	56	100	1588.7	870.3	0.45	0.2	34
LDH@NG	No	-	0.3	1.2	63	1000	709	337	0.034	2.0	35
Ni <sub>3</sub> (HITP) <sub>2</sub> /PP	No	-	0.066	3.5	63.2	500	851	716	0.032	1.0	36
Nafion	No	-	0.7	0.53	50	500	800	480	0.08	1.0	37
MWCNTs/NCQDs	No	-	0.15	1.3-1.5	60	500	1274.8	956.1	0.05	1.0	38
G/MnO <sub>2</sub> @CNT	No	-	0.104	1.1	60	2500	~1065	293	0.029	1.0	39

## References

1. Y. Yang, B. Li, L. Li, S. Seeger and J. Zhang, *iScience*, 2019, **16**, 420-432.
2. Y. He, Z. Chang, S. Wu, Y. Qiao, S. Bai, K. Jiang, P. He and H. Zhou, *Adv. Energy Mater.*, 2018, **8**, 1802130.
3. E. Cha, M. D. Patel, J. Park, J. Hwang, V. Prasad, K. Cho and W. Choi, *Nat. Nanotechnol.*, 2018, **13**, 337-344.
4. X. B. Cheng, R. Zhang, C. Z. Zhao and Q. Zhang, *Chem. Rev.*, 2017, **117**, 10403-10473.
5. Y. Liu, Q. Liu, L. Xin, Y. Liu, F. Yang, E. A. Stach and J. Xie, *Nat. Energy*, 2017, **2**, 17083.
6. C. Li, S. Liu, C. Shi, G. Liang, Z. Lu, R. Fu and D. Wu, *Nat. Commun.*, 2019, **10**, 1363.
7. C. Z. Zhao, P. Y. Chen, R. Zhang, X. Chen, B. Q. Li, X. Q. Zhang, X. B. Cheng and Q. Zhang, *Sci. Adv.* 2018, **4**, eaat3446.
8. Q. Pang, X. Liang, C. Y. Kwok and L. F. Nazar, *Nat. Energy*, 2016, **1**, 16132.
9. Z. Wang, F. Guo, C. Chen, L. Shi, S. Yuan, L. Sun and J. Zhu, *ACS Appl. Mater. Interfaces*, 2015, **7**, 3314-3322.
10. S. Wei, S. Choudhury, Z. Tu, K. Zhang and L. A. Archer, *Acc. Chem. Res.*, 2018, **51**, 80-88.
11. J. Wu, H. Zeng, X. Li, X. Xiang, Y. Liao, Z. Xue, Y. Ye and X. Xie, *Adv. Energy Mater.*, 2018, **8**, 1802430.
12. Y. Yang and J. Zhang, *Adv. Energy Mater.*, 2018, **8**, 1801778.
13. T. Yim, S. H. Han, N. H. Park, M. S. Park, J. H. Lee, J. Shin, J. W. Choi, Y. Jung, Y. N. Jo, J. S. Yu and K. J. Kim, *Adv. Funct. Mater.*, 2016, **26**, 7817-7823.
14. Y. Luo, N. Luo, W. Kong, H. Wu, K. Wang, S. Fan, W. Duan and J. Wang, *Small*, 2017, **14**, 1702853.
15. J. Sun, Y. Sun, M. Pasta, G. Zhou, Y. Li, W. Liu, F. Xiong and Y. Cui, *Adv. Mater.*, 2016, **28**, 9797-9803.
16. Z. A. Ghazi, X. He, A. M. Khattak, N. A. Khan, B. Liang, A. Iqbal, J. Wang, H. Sin, L. Li and Z. Tang, *Adv. Mater.*, 2017, **29**, 1606817.
17. J. Yoo, S. J. Cho, G. Y. Jung, S. H. Kim, K. H. Choi, J. H. Kim, C. K. Lee, S. K. Kwak and

- S. Y. Lee, *Nano Lett.*, 2016, **16**, 3292-3300.
18. P. J. H. Kim, J. Seo, K. Fu, J. Choi, Z. Liu, J. Kwon, L. Hu and U. Paik, *NPG Asia Mater.*, 2017, **9**, e375.
19. Y. Mao, G. Li, Y. Guo, Z. Li, C. Liang, X. Peng and Z. Lin, *Nat. Commun.*, 2017, **8**, 14628.
20. Z. Cui, C. Zu, W. Zhou, A. Manthiram and J. B. Goodenough, *Adv. Mater.*, 2016, **28**, 6926-6931.
21. L. Ma, H. L. Zhuang, S. Wei, K. E. Hendrickson, M. S. Kim, G. Cohn, R. G. Hennig and L. A. Archer, *ACS Nano*, 2016, **10**, 1050-1059.
22. F. Pei, T. An, J. Zang, X. Zhao, X. Fang, M. Zheng, Q. Dong and N. Zheng, *Adv. Energy Mater.*, 2016, **6**, 1502539.
23. Z. Zheng, H. Guo, F. Pei, X. Zhang, X. Chen, X. Fang, T. Wang and N. Zheng, *Adv. Funct. Mater.*, 2016, **26**, 8952-8959.
24. Y. J. Li, J. M. Fan, M. S. Zheng and Q. F. Dong, *Energy Environ. Sci.*, 2016, **9**, 1998-2004.
25. Q. Pang and L. F. Nazar, *ACS Nano*, 2016, **10**, 4111-4118.
26. J. Zhang, H. Hu, Z. Li and X. W. Lou, *Angew. Chem. Int. Ed.*, 2016, **55**, 3982-3986.
27. Z. Li, J. Zhang and X. W. Lou, *Angew. Chem. Int. Ed.*, 2015, **54**, 12886-12890.
28. G. Zhou, Y. Zhao and A. Manthiram, *Adv. Energy Mater.*, 2015, **5**, 1402263.
29. W. Zhou, B. Guo, H. Gao and J. B. Goodenough, *Adv. Energy Mater.*, 2016, **6**, 1502059.
30. G. Zhou, E. Paek, G. S. Hwang and A. Manthiram, *Nat. Commun.*, 2015, **6**, 7760.
31. F. Pei, L. Lin, A. Fu, S. Mo, D. Ou, X. Fang and N. Zheng, *Joule*, 2018, **2**, 323-336.
32. Y. Zhao, M. Liu, W. Lv, Y. B. He, C. Wang, Q. Yun, B. Li, F. Kang and Q. H. Yang, *Nano Energy*, 2016, **30**, 1-8.
33. S. Bai, X. Liu, K. Zhu, S. Wu and H. Zhou, *Nat. Energy*, 2016, **1**, 16094.
34. F. Wu, S. Zhao, L. Chen, Y. Lu, Y. Su, Y. Jia, L. Bao, J. Wang, S. Chen and R. Chen, *Energy Storage Mater.*, 2018, **14**, 383-391.
35. H. J. Peng, Z. W. Zhang, J. Q. Huang, G. Zhang, J. Xie, W. T. Xu, J. L. Shi, X. Chen, X. B. Cheng and Q. Zhang, *Adv. Mater.*, 2016, **28**, 9551-9558.

36. Y. Zang, F. Pei, J. Huang, Z. Fu, G. Xu and X. Fang, *Adv. Energy Mater.*, 2018, **8**, 1802052.
37. J. Q. Huang, Q. Zhang, H. J. Peng, X. Y. Liu, W. Z. Qian and F. Wei, *Energy Environ. Sci.*, 2014, **7**, 347-353.
38. Y. Pang, J. Wei, Y. Wang and Y. Xia, *Adv. Energy Mater.*, 2018, **8**, 1702288.
39. W. Kong, L. Yan, Y. Luo, D. Wang, K. Jiang, Q. Li, S. Fan and J. Wang, *Adv. Funct. Mater.*, 2017, **27**, 1606663.